



The effect of hydrogen content and yield strength on the distribution of hydrogen in steel: a diffusion coupled micromechanical FEM study

Abdelrahman Hussein^a, Alfons H.M. Krom^b, Poułumi Dey^c, Gagus K. Sunnardianto^{c,d}, Othonas A. Moults^e, Carey L. Walters^{a,*}

^a Maritime and Transport Technology Department, Faculty of Mechanical, Maritime and Materials Engineering, Delft University of Technology, Mekelweg 2, 2628 CD Delft, The Netherlands

^b Safety Department, N.V. Nederlandse Gasunie, Concourslaan 17, 9727 KC Groningen, The Netherlands

^c Materials Science and Engineering Department, Faculty of Mechanical, Maritime and Materials Engineering, Delft University of Technology, Mekelweg 2, 2628 CD Delft, The Netherlands

^d Research Center for Physics, Indonesian Institute of Sciences, Kawasan Puspitek Serpong, Tangerang Selatan, 15314, Banten, Indonesia

^e Engineering Thermodynamics, Process & Energy Department, Faculty of Mechanical, Maritime and Materials Engineering, Delft University of Technology, Leeghwaterstraat 39, 2628 CB Delft, The Netherlands



ARTICLE INFO

Article history:

Received 23 December 2020

Revised 20 February 2021

Accepted 6 March 2021

Available online 15 March 2021

Keywords:

Hydrogen embrittlement

Hydrogen diffusion

Crystal plasticity

Representative volume element

Micromechanical modeling

ABSTRACT

In this study, we investigate the effect of the heterogeneous micromechanical stress fields resulting from the grain-scale anisotropy on the redistribution of hydrogen using a diffusion coupled crystal plasticity model. A representative volume element with periodic boundary conditions was used to model a synthetic microstructure. The effect of tensile loading, initial hydrogen content and yield strength on the redistribution of lattice (C_L) and dislocation trapped (C_x) hydrogen was studied. It was found that the heterogeneous micromechanical stress fields resulted in the accumulation of both populations primarily at the grain boundaries. This shows that in addition to the well-known grain boundary trapping, the interplay of the heterogeneous micromechanical hydrostatic stresses and plastic strains contribute to the accumulation of hydrogen at the grain boundaries. Higher yield strength reduced the amount of C_x due to the resulting lower plastic deformation levels. On the other side, the resulting higher hydrostatic stresses increased the depletion of C_L from the compressive regions and its diffusion toward the tensile ones. These regions with increased C_L are expected to be potential damage initiation zones. This aligns with the observations that high-strength steels are more susceptible to hydrogen embrittlement than those with lower-strength.

© 2021 The Authors. Published by Elsevier Ltd on behalf of Acta Materialia Inc. This is an open access article under the CC BY license (<http://creativecommons.org/licenses/by/4.0/>)

1. Introduction

The use of hydrogen as an energy carrier is a main milestone for achieving widespread green and sustainable energy [1]. One of the challenges to realize this milestone is establishing reliable and safe structures for transporting hydrogen [2]. Metals in contact with hydrogen are well known to suffer from loss of integrity known as hydrogen embrittlement (HE) [3–6]. Several mechanisms can lead to HE; however, for steels, it is widely accepted that two main mechanisms dominate: hydrogen enhanced decohesion (HEDE) and hydrogen enhanced localized plasticity (HELP) [7]. The underlying principle of HEDE is that a threshold of hydrogen con-

centration will reduce the cohesive strength between the metal atoms. When these atoms are interface atoms (grain boundaries, carbides, secondary phases etc.), the characteristic intergranular damage of HE occurs, which was recently termed "IG-HEDE" [8]. This is to distinguish it from the less common transgranular decohesion "T-HEDE" in the bulk atoms. The other mechanism HELP, is based on the assumption that hydrogen interaction with dislocations increases their mobility [9]. Macroscopically, this results in plastic softening and shear localization [10]. Another scenario is that hydrogen shields the interaction among dislocations, allowing their pile-up along interfaces and leading to their decohesion [11,12].

Although HE has been studied for many decades [13], a general mechanistic explanation is lacking. This is due to the synergistic operation of multiple mechanisms outlined above promoted by the wide range of steel microstructures [7,14–16]. A step toward

* Corresponding author.

E-mail addresses: a.h.a.hussein@tudelft.nl (A. Hussein), c.l.walters@tudelft.nl (C.L. Walters).

discerning the interaction of these mechanisms is to understand the hydrogen distribution and the driving forces behind it. Total hydrogen concentration (C_{tot}) can be partitioned into lattice (C_L) and trapped (C_x) concentrations [17–19]. C_L resides at the interstitial lattice sites, while C_x can be trapped in imperfections like vacancies, dislocations, interfaces etc. The driving force for hydrogen diffusion, the difference in chemical potential, depends not only on the concentration but also on the hydrostatic stresses. Hydrostatic stress gradient drives hydrogen from compressive to tensile regions. Following Oriani [20], trapped hydrogen and lattice hydrogen are in equilibrium. Limiting our discussion to dislocation traps, the density of trap sites stems from the dislocation density, which evolves with plastic deformation. This highlights the importance of considering mechanical loading when analysing the hydrogen distribution.

Being the smallest atom in the periodic table, hydrogen has very fast diffusivity and low interaction with electrons making it difficult to measure using electron microscopy [21]. Probing hydrogen with high spatial resolution is a technical challenge [21–23] especially for samples under stress. Several studies used diffusion coupled mechanics models to study the effect of stresses at a crack tip [18,24–27]. Although they provided very useful insights on the distribution of hydrogen at the crack tip, they were unable to provide detailed insights at the microstructural level. Therefore, more knowledge is needed into how hydrogen is distributed between lattice and trapped hydrogen concentrations, which is critical in understanding the competition between different HE modes.

It is well known from empirical observations that high-strength steels are more sensitive to HE than lower-strength steels [28,29]. However, it is impossible to separate the effects of grain size, composition, yield strength, local mechanical loading, and other factors in experimental studies because these cannot be independently controlled in real steels. Therefore, the different contributions of these effects remain unknown. An appealing way to resolve these questions is to use micromechanics based finite element method (FEM). In this approach, an artificial microstructure is generated using representative volume element (RVE) [30]. Recently, several studies reported the effect of polycrystalline anisotropy on the hydrogen distribution using RVE and crystal plasticity model. Ilin *et al.* [31] investigated the effect of mechanical loading and grain boundary trapping in 316L stainless steel. They found that hydrogen accumulates at regions with high hydrostatic stresses while trapping had negligible effect. Hassan *et al.* [32] modeled a RVE under biaxial loading and came to similar conclusions. It is worth noting that in both studies, very large initial hydrogen content was used. Charles *et al.* [33] studied the diffusivity by permeating hydrogen in a predeformed synthetic polycrystal.

In this study, we use a RVE and diffusion coupled crystal plasticity FEM to investigate how the yield strength, grain-scale anisotropy, and mechanical loading impact the sensitivity to hydrogen embrittlement and the localized distribution of lattice and trapped hydrogen in the absence of grain boundary trap. This is done by simulating the effect of the stresses on the redistribution of hydrogen at the microstructural scale in α -iron. A synthetic microstructure subjected to plane strain tensile load was modeled using a periodic RVE with randomly oriented grains. The heterogeneous deformation resulting from the polycrystalline anisotropy was modeled using crystal plasticity. Dislocations were used as the trapping sites in the hydrogen transport model. Understanding the relative partitioning of C_L and C_x can aid in identifying the type of hydrogen population, and thus, the possible HE triggering mechanism [6,25,34]. We elucidate the effect of initial hydrogen content on this partitioning. A statistical analysis was performed in order to quantitatively address the partitioning of both populations. Furthermore, it is well known that high strength steels are especially susceptible to HE [28,29]. In order to shed light on this behavior,

we investigate the effect of higher yield strength on the redistribution pattern of hydrogen.

2. Computational model

2.1. Representative volume element and grain morphology

The workflow for artificial microstructure, or RVE, generation involves four steps: geometry generation, generation of synthetic orientations, meshing and pre-processing. The artificial grain morphology was generated using an in-house MATLAB script for periodic Voronoi tessellation. The synthetic orientations and all the subsequent crystallographic analysis was performed using the open source code MTEX [35]. For meshing we used the open source code Gmsh [36]. The preprocessing for ABAQUS was performed using a python script for imposing periodic boundary conditions and assigning grain orientations and properties. The Voronoi tessellation is a widely used method for the geometric representation of polycrystals [30,37]. In 2D, Voronoi tessellation is the partitioning of a plane domain into n convex polygons based on a predetermined distribution of n points or seeds. All the points within a polygon are closer to the polygon's seed than the seeds of other polygons. In this work, the plane domain boundary is a square. To use smaller RVEs with the minimal impact on the accuracy of the results, periodic geometry was used. Together with periodic boundary conditions (PBCs), described in details in section 2.2, the RVEs correspond to infinitely repeating microstructure. Physically, these geometric processes represent a crystallization process where all seeds concurrently nucleate and grow isotropically in 2D.

The morphology of the grains (relative size and shape) can be controlled by controlling the number and distribution of the seed points within the enclosing domain. In order to improve Voronoi tessellation uniformity and reduce extreme aspect ratios, the Voronoi seed points were sampled from a Halton sequence [38]. A RVE with an edge size of 500 μm is shown in Fig. 1(a). The corresponding grain area histogram is shown in Fig. 1(b). Random orientations were assigned to the grains. First, an orientation distribution function (ODF) was generated in MTEX. Then individual orientations were randomly sampled from this ODF and assigned to each grain. It should be noted that periodic grains at the boundary edges were assigned similar orientations in order to maintain microstructure periodicity. The {100}, {110} and {111} pole-figures of these sampled orientations are shown in Fig. 1(c). To assess the randomness of the orientations, a misorientation distribution function (MDF) was fitted to the sampled orientations. A plot of the MDF in Fig. 1(d) clearly shows a Mackenzie distribution, confirming the randomness of the orientations. The RVE geometry is then meshed with second-order six-node triangular elements using Gmsh.

2.2. Periodic boundary conditions

The application of PBCs results in a compatible deformation of each pair of opposite boundary edges, i.e. have identical shape during deformation. For implementing such boundary conditions, periodic nodes (red circles in Fig. 2) on opposite edges of the bounding square were enforced during the meshing process. Finally, the mesh file was pre-processed within ABAQUS using a python script to assign material properties and apply PBCs to the boundary nodes. Here we adopt the implementation described in [39–41]. This can be summarized as follows. The vertex nodes V_{1-4} (yellow circles in Fig. 2) are defined by the intersection of two edges, and thus, will have a different formulation from the inner edge nodes (red circles in Fig. 2) and are retained for load application. V_1 is a fixed node, while in-plane displacements u_i in directions 1 and 2 can be applied through V_2 and/or V_4 to result in the

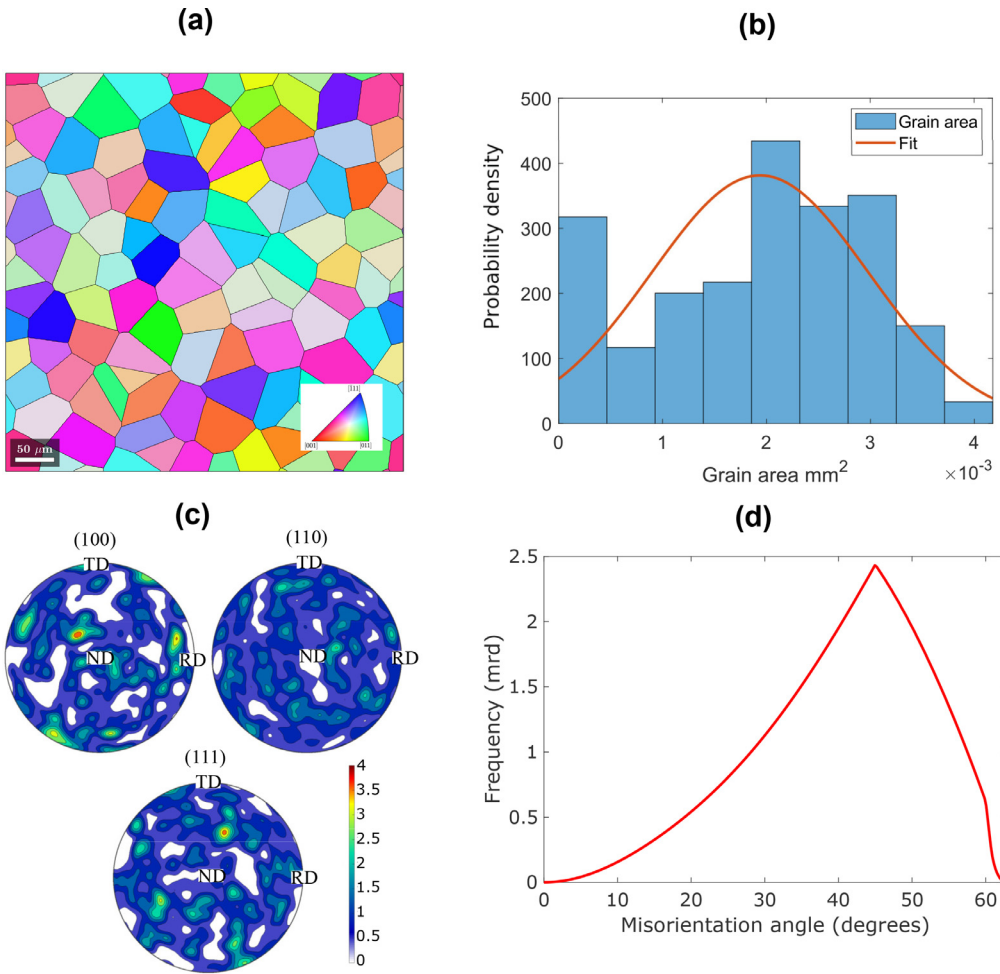


Fig. 1. Morphology and orientation distribution in a RVE: (a) An example RVE showing grain morphology color coded according to orientations from inverse pole figure. (b) Histogram of the grain area distribution. (c) {100},{110} and {111} pole figures of the orientations assigned to the RVE. (d) Misorientation distribution.

desired loading state. V_3 is not independent and its deformation is kinematically tied to the other vertices as

$$u_i^{V_1} - u_i^{V_2} - u_i^{V_3} + u_i^{V_4} = 0, \quad i = 1, 2 \quad (1)$$

In this study, we apply uniaxial far-field strain $\bar{\epsilon}_{22}$ in direction 2 on a RVE with an edge length l . This can be formulated as

$$\begin{aligned} u_2^{V_4} - u_2^{V_1} &= \bar{\epsilon}_{22} l \\ u_2^{V_2} - u_2^{V_1} &= 0 \end{aligned} \quad (2)$$

Since $u_1^{V_1} = u_2^{V_1} = 0$, the displacement boundary conditions on nodes V_4 and V_2 become

$$\begin{aligned} u_2^{V_4} &= \bar{\epsilon}_{22} l \\ u_2^{V_2} &= 0 \end{aligned} \quad (3)$$

The displacement degrees of freedom $u_i(x, y)$ of the inner edge nodes on each pair of opposite edges are kinematically linked to the vertex nodes V_1 , V_2 and V_4 as

$$\begin{aligned} u_i(y, x=0) - u_i(y, x=l) - u_i^{V_2} + u_i^{V_1} &= 0 \\ u_i(x, y=0) - u_i(x, y=l) - u_i^{V_4} + u_i^{V_1} &= 0 \end{aligned} \quad i = 1, 2 \quad (4)$$

where x and y are the coordinates of the boundary nodes. In ABAQUS, Eq. (1) and (4) are implemented as *linear constraint equations* on the boundary nodes.

2.3. Crystal plasticity model

A crystal plasticity model [42] is used for the mechanical behaviour of individual grains. A finite strain framework where the

multiplicative decomposition of the total deformation gradient \mathbf{F} into elastic \mathbf{F}^* and plastic \mathbf{F}^p parts as

$$\mathbf{F} = \mathbf{F}^* \cdot \mathbf{F}^p \quad (5)$$

A slip system α in the initial configuration is defined by its slip direction \mathbf{s}^α and normal to the slip plane \mathbf{m}^α . Here, we assume the 12 slip systems $\{110\}\langle\bar{1}11\rangle$ in BCC iron as the active slip systems for simplicity. In the deformed configuration they are given by

$$\begin{aligned} \mathbf{s}^{*\alpha} &= \mathbf{F}^* \cdot \mathbf{s}^\alpha \\ \mathbf{m}^{*\alpha} &= \mathbf{m}^\alpha \cdot \mathbf{F}^{*-1} \end{aligned} \quad (6)$$

The evolution of the slip rate $\dot{\gamma}$ is modeled using the classical viscoplastic formulation [43]

$$\dot{\gamma}^\alpha = \dot{a}_0^\alpha \left(\frac{\tau^\alpha}{g^\alpha} \right) \left| \frac{\tau^\alpha}{g^\alpha} \right|^{n-1} \quad (7)$$

where \dot{a}_0^α is the reference strain on slip system α , τ^α is the resolved shear stress, or Schmid stress, on that system and g^α is the function describing its current strength. τ^α is expressed as

$$\tau^\alpha = \frac{1}{2} (\mathbf{s}^{*\alpha} \otimes \mathbf{m}^{*\alpha} + \mathbf{m}^{*\alpha} \otimes \mathbf{s}^{*\alpha}) : \boldsymbol{\tau} \quad (8)$$

where $\boldsymbol{\tau}$ is the Kirchhoff stress. The current strengths g^α evolve as

$$\dot{g}^\alpha = \sum_\beta h_{\alpha\beta} \dot{\gamma}^\beta \quad (9)$$

where the summation is over all the active slip systems β . $h_{\alpha\beta}$ is the matrix of the hardening moduli with the diagonal terms

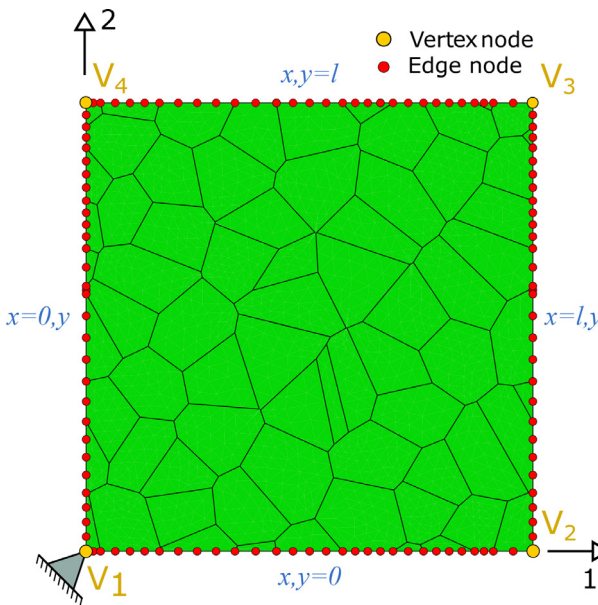


Fig. 2. Illustration of the periodic boundary conditions, boundary nodes and their nomenclature.

Table 1

Crystal plasticity model parameters for α -iron [44]

Cubic elasticity constants	Flow and hardening parameters
C_{11} 236.9 GPa	Reference strain rate $\dot{\epsilon}_0$ 10^{-3} s^{-1}
C_{12} 140.6 GPa	Rate sensitivity exponent n 50
C_{44} 116 GPa	Initial critical resolved shear stress τ_0 30 MPa
	Initial hardening modulus h_0 170 MPa
	Saturation stress τ_s 90 MPa
	Ratio of latent to self hardening q 1.1

$h_{\alpha\alpha}$ (no summation) are called self-hardening moduli and the off-diagonal terms $h_{\alpha\beta}$ ($\alpha \neq \beta$) are called latent-hardening moduli. A simple form for self-hardening is given by Pierce, Asaro and Needleman [43]

$$h_{\alpha\alpha}(\gamma) = h_0 \operatorname{sech}^2 \left| \frac{h_0 \gamma}{\tau_s - \tau_0} \right|, \text{ no summation on } \alpha \quad (10)$$

where h_0 is the initial hardening modulus, τ_s is the saturation stress and τ_0 is the initial critical resolved shear stress. γ is the cumulative shear strain on all slip systems

$$\gamma = \varepsilon_p = \sum_{\alpha} \int_0^t |\dot{\gamma}^{\alpha}| dt \quad (11)$$

The latent hardening is calculated as

$$h_{\alpha\beta} = q h_{\alpha\alpha}(\gamma), \alpha \neq \beta \quad (12)$$

where q is the ratio of latent to self-hardening. The parameters of single crystal α -iron were obtained by calibrating the crystal plasticity model with the results from Franciosi *et al.* [44] are shown in Table 1. It was implemented in ABAQUS as a user defined material (UMAT) subroutine developed by Huang [42,45] and further modified to be compatible with the hydrogen transport model as discussed next.

2.4. Hydrogen transport model

Here we use the hydrogen transport model of Sofronis and McMeeking [18] to include the effect of trapping and hydrostatic stress, and later improved by Krom *et al.* [24] to include the effect of plastic strain rate. This model assumes only dislocations as trap

sites, which are saturable and reversible. The molar concentration (mol/mm^3) of hydrogen in lattice sites

$$C_L = N_L \theta_L \quad (13)$$

where N_L is the number of solvent atoms per unit lattice volume and θ_L is the fractional occupancy of lattice sites. Similarly, the trapped hydrogen concentration

$$C_x = N_x \theta_x \quad (14)$$

where N_x is the number of trap sites per unit volume and θ_x is the fractional occupancy of trap sites. The trapped C_x is not independent of the mobile C_L , and indeed, there is a local equilibrium between both populations. Oriani [20] expressed the local equilibrium between both populations as

$$\frac{\theta_x}{1 - \theta_x} = \theta_L K_T = \theta_L \exp \left(\frac{-W_B}{RT} \right) \quad (15)$$

where K_T is the trap equilibrium constant, W_B is the trap binding energy, R is the universal gas constant and T is the absolute temperature. Krom and Bakker [17] showed that this condition can be assumed for strain rates less than 1 s^{-1} . Combining Eq. 13-(15)

$$C_x = \frac{N_x}{1 + \frac{N_L}{K_T C_L}} \quad (16)$$

Assuming that hydrogen diffuses only through lattice sites, the hydrogen mass transport equation can be expressed as

$$\frac{\partial(C_L + C_x)}{\partial t} - \nabla \cdot \mathbf{J}_L = 0 \quad (17)$$

where \mathbf{J}_L is the lattice hydrogen flux. For a system under external loading, the hydrostatic stress term σ_H in the chemical potential is not constant. High hydrostatic stresses will reduce the chemical potential and result in an influx of hydrogen from regions with compressive hydrostatic stresses to regions with tensile hydrostatic stresses. This can be formulated in the lattice hydrogen flux as

$$\mathbf{J}_L = -D_L \nabla C_L + \frac{D_L C_L \bar{V}_H}{RT} \nabla \sigma_H \quad (18)$$

where D_L is the lattice-diffusion coefficient, \bar{V}_H is the partial molar volume of hydrogen and $\nabla \sigma_H$ is the gradient of the hydrostatic stress. As mentioned previously, in this study, we only consider dislocations as trapping sites. Kumnick and Johnson [46] studied the evolution of trap site density in terms of plastic deformation. While their model is empirical in nature, it has been recently combined with RVE-level simulations (e.g. [32,33]) to provide insight into micromechanical behavior. They found a sharp increase in trap site density in the initial levels of plastic deformation which saturates gradually with further deformation. A fit of their results as a function of the equivalent plastic strain ε_p is

$$\log_{10} N_x = 23.26 - 2.33 \exp(-5.5 \varepsilon_p) \quad (19)$$

The time derivative of the trap site concentration can then be expressed as [17]

$$\frac{\partial C_x}{\partial t} = \frac{\partial C_x}{\partial C_L} \frac{\partial C_L}{\partial t} + \theta_x \frac{dN_x}{d\varepsilon_p} \frac{d\varepsilon_p}{dt} \quad (20)$$

From Eq. (16)

$$\frac{\partial C_x}{\partial C_L} = \frac{C_x(1 - \theta_x)}{C_L} \quad (21)$$

Using Eq. (18), (20) and (21), the mechanics coupled hydrogen mass transport Eq. (17) becomes

$$\frac{D_L}{D_{eff}} \frac{\partial C_L}{\partial t} + \nabla \cdot \left(-D_L \nabla C_L + \frac{D_L C_L \bar{V}_H}{RT} \nabla \sigma_H \right) + \theta_x \frac{dN_x}{d\varepsilon_p} \frac{d\varepsilon_p}{dt} \quad (22)$$

Table 2
Material parameters for hydrogen diffusion in α -iron [24]

Quantity	Value
Diffusion coefficient D_L	$1.27 \times 10^{-2} \text{ mm}^2/\text{s}$
Occupancy of lattice sites N_L	$8.46 \times 10^{-4} \text{ mol/mm}^3$
Molar volume of hydrogen \bar{V}_H	$2 \times 10^3 \text{ mm}^3/\text{mol}$
Trap binding energy W_B	-60 kJ/mol
Temperature T	300 K
Universal gas constant R	8.31 J/molK

The term D_{eff} in Eq. (22) is called the effective diffusivity and is given by

$$D_{eff} = \frac{D_L}{\left(1 + \frac{\partial C_x}{\partial C_L}\right)} = \frac{D_L C_L}{C_L + C_x(1 - \theta_x)} \quad (23)$$

The material parameters used for the hydrogen transport analysis are summarized in Table 2. Eq. (22) is a non-standard mass transport equation, and its implementation in commercial FEM software requires a special treatment. Oh et al. [47] took advantage of the analogy between heat and mass transfer to implement Eq. (22) in ABAQUS using user-defined thermal material (UMATHT) subroutine. Several works implemented the same methodology for hydrogen transport analysis both at the macroscale [48–50] and the RVE level [32,33,51]. A detailed discussion on the implementation can be found in [47,49]. Furthermore, the solution of Eq. (22) requires the calculation of the hydrostatic stress gradient terms $\nabla \sigma_H$, which are obtained from the UMAT subroutine as discussed in the appendix. For solving this coupled mechanics-diffusion problem, second order triangular elements CPE6MT were used for the coupled analysis in ABAQUS.

2.5. Initial hydrogen concentration and loading

The initial partitioning of both C_L and C_x depends on the initial hydrogen concentration, initial trap site concentration N_x and the trap binding energy W_B . At equilibrium and for stress-free samples, the solubility of hydrogen in the lattice sites, which for an initial value problem is evaluated as the initial lattice concentration C_{Lo} [18,24], can be calculated from Sieverts' law as [52]

$$C_{Lo} = k\sqrt{p} \quad (24)$$

where p is the hydrogen gas pressure, and the solubility of hydrogen $k = k_0 \exp(-\Delta H_s/RT)$. k_0 is a constant and $-\Delta H_s$ is the enthalpy of solution with the values $0.82 \text{ mol}/(\text{m}^3\text{Pa}^{1/2})$ and 28.6 kJ/mol respectively for hydrogen in iron. At large hydrogen gas pressures, the pressure in Eq. (24) must be replaced with the fugacity [53] such that

$$C_{Lo} = k\sqrt{f} = k\sqrt{p \exp\left(p\left(\frac{z_1}{T} + z_2\right)\right)} \quad (25)$$

where $z_1 = 1.51 \times 10^{-6} \text{ K/Pa}$ and $z_2 = -1.04 \times 10^{-11} \text{ Pa}^{-1}$ are fitting coefficients [53]. A plot of Eq. (24) and (25) is shown in Fig. 3. It can be seen that hydrogen pressures of up to 100 bar, both values almost coincide. In this study, we chose hydrogen pressures of 1, 100, 200 and 1000 bar, and their corresponding C_{Lo} was calculated using Eq. (25). From a practical point of view, pressures of 200 bar are observed in the petrochemical industries, and for future use in energy transport, hydrogen pressure of 1000 bar is being considered to maximise the energy density to a practical level [54]. The corresponding values of C_{Lo} are shown in Table 3.

Unless otherwise mentioned, we assume that all samples are precharged under equilibrium conditions. The corresponding initial trap site concentration C_{xo} can be calculated from Eq. (16) and (19) with $\varepsilon_p = 0$. The total initial concentration is then $C_{tot0} = C_{Lo} +$

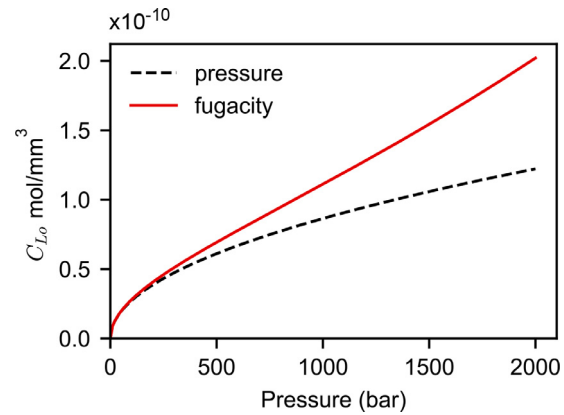


Fig. 3. The effect of pressure and fugacity on the equilibrium initial lattice concentration C_{Lo} of unstressed sample at 300 K.

Table 3

Boundary hydrogen gas pressure p and the corresponding initial lattice concentration C_{Lo} according to Eq. (25) at 300 K.

Pressure bar	Initial lattice site concentration C_{Lo} mol/mm ³
1	2.735×10^{-12}
100	2.804×10^{-11}
200	4.066×10^{-11}
1000	1.112×10^{-10}

C_{Lo} . A far-field plane strain tensile loading of $\dot{\varepsilon}_{22} = 3 \times 10^{-2}$ was applied to the RVE over the duration of 100 s, which corresponds to a strain rate of $3 \times 10^{-4} \text{ s}^{-1}$. The hydrogen concentration at the boundary of the RVE was maintained constant during the loading. This corresponds to tensile testing under constant hydrogen gas pressure [55] allowing for increasing the hydrogen content in the model.

3. Results and discussion

3.1. Effect of hydrogen gas charging pressure

Upon loading, a heterogeneous distribution of stress and strain within the RVE develops due to the randomly distributed misorientations and the grain-scale elastic and plastic anisotropy. This results in the redistribution of the initially uniformly distributed hydrogen as shown in Fig. 4. This concentration distribution does not change with increasing the period over which the load is applied. Our results (not shown here for brevity) showed that increasing the loading time up to 3000 s did not show a significant change in the hydrogen concentration, indicating a steady state condition. This is due to the very fast diffusion of hydrogen in iron as well as the relatively smaller length scale of RVE computations compared to structural scale models. In order to discuss these effects, a detailed study accounting for the rate dependent parameters like diffusion coefficient, loading rate and viscoplastic effects is under investigation.

Fig. 4 (a & b) show that the lattice hydrogen C_L diffuses toward regions with tensile hydrostatic stresses and depletes from regions with compressive hydrostatic stresses. These values deviate from the initial concentrations shown in Table 3. For both cases, these regions are primarily the grain boundary triple points. On the other side, the trapped hydrogen C_x accumulates at regions of large plastic strains. Fig. 4(c & d) shows that these regions form bands of approximately 45° to the loading direction, which is to be expected for plastic shear bands. The intensity of these bands is maximum along the grain boundaries, which manifests the accumulation of hydrogen due to dislocation pile-up [11]. Furthermore, the effect of

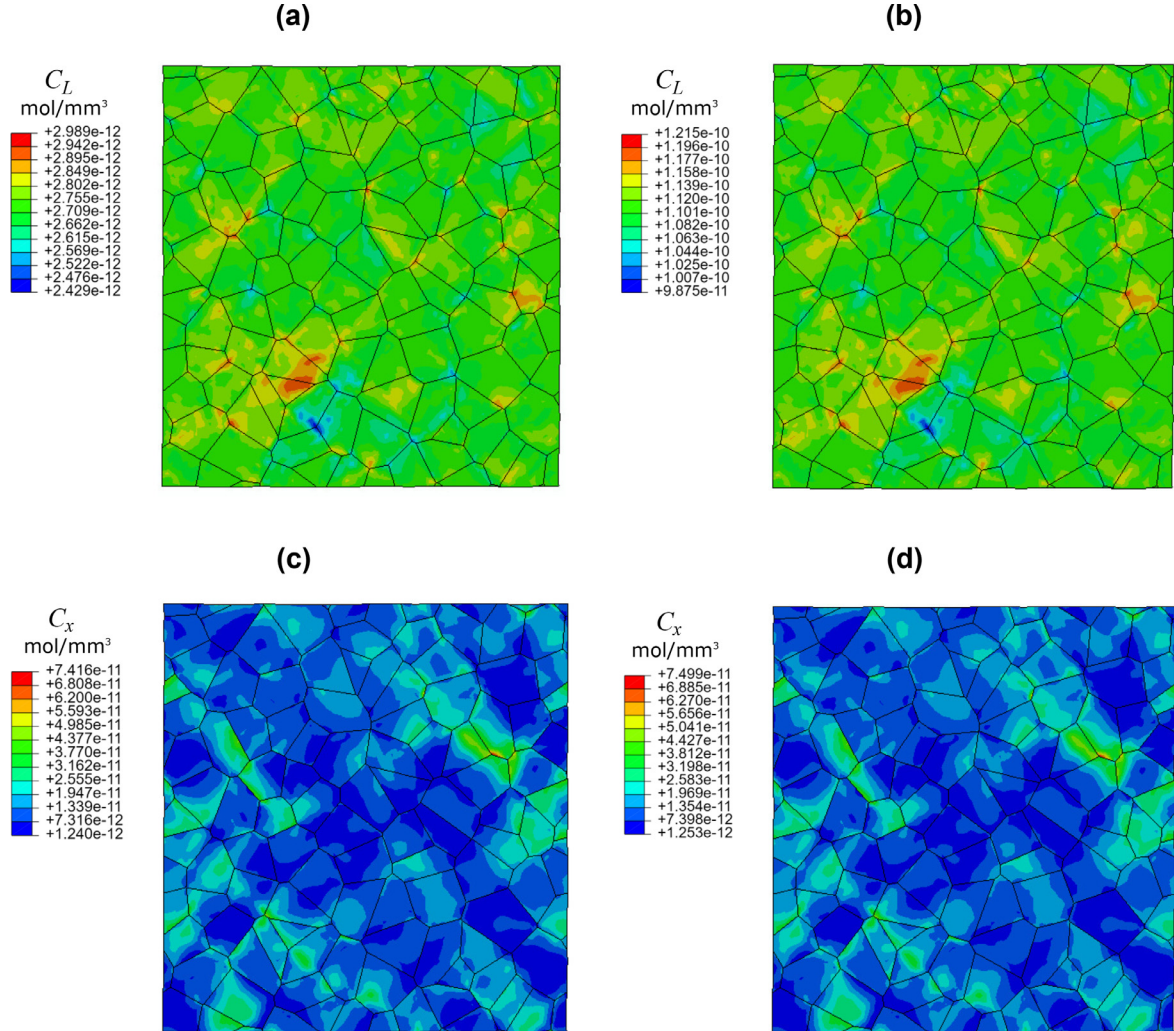


Fig. 4. The lattice hydrogen C_L distribution within the RVE after 3×10^{-2} tensile strain loading corresponding to hydrogen pressure of (a) 1 bar and (b) 1000 bar. Note the difference in the range of the legend in both cases. The associated trapped hydrogen C_x at (c) 1 bar and (d) 1000 bar.

geometrically necessary dislocations (GNDs) on the hydrogen distribution at a crack tip has been recently reported [56]. Kumar and Mahajan [51] showed that strain gradients lead to the accumulation of GND trapped hydrogen at the grain boundaries.

Next, we discuss the influence of the hydrogen pressure, i.e. the initial hydrogen concentration C_{tot_0} , on the partitioning of lattice and trap site concentrations. This is an important factor in understanding the relative contribution of each population to HE. The distribution of lattice hydrogen within the RVE at 1 bar and 1000 bar are shown in Fig. 4(a) and (b) respectively. It can be seen that the distribution in both cases is almost identical, except that the quantities are two orders of magnitudes higher for the 1000 bar case. This behaviour is expected, as the loading conditions and the RVE parameters were kept constant, while the only variable is the hydrogen pressure according to Eq. (25). A quantification of this behaviour can be achieved through the distribution of probability density of the integration point values of C_L as shown in the first row of Fig. 5 for different hydrogen pressures. C_L shows a normal distribution that is almost identical in shape, i.e. its relative standard deviation (RSD) is constant and is approximately 1.75%. However, the mean of the distribution increases with increasing the charging pressure from $2.69 \times 10^{-12} \text{ mol/mm}^3$ for 1 bar up to $1.09 \times 10^{-10} \text{ mol/mm}^3$ for 1000 bar.

In the case of trapped hydrogen, the distributions are similar and there is only a negligible increase in the magnitudes for both pressures as shown in Fig. 4(c & d). The probability density distribution of C_x is shown in the second row of Fig. 5. C_x has a log-normal distribution which maintains its shape (RSD = 69.23%) and mean of approximately $1.31 \times 10^{-11} \text{ mol/mm}^3$ with increasing hydrogen pressure. As plastic deformation increases, more dislocations are created, and consequently more trap sites according to Eq. (19). Hydrogen diffuses to fill in these trap sites, while maintaining equilibrium with C_L . Due to the strong binding energy of -60 kJ/mol , C_x is strongly dependent on ε_p and its dependence on C_L using Oriani's hypothesis in Eq. (15) is negligible. Weaker dislocation trap binding energies, between -40 and -20 kJ/mol , for different types of steels have been investigated [25,34]. How this might affect C_x is a subject of future analysis.

The effect of the loading on the hydrogen uptake for both hydrogen populations can be represented by the mean value of the distributions. The mean values for C_L are 2.69×10^{-12} , 2.76×10^{-11} , 4.01×10^{-11} and $1.09 \times 10^{-10} \text{ mol/mm}^3$ for hydrogen pressures of 1, 100, 200 and 1000 bar respectively. These values are approximately equal to the initial lattice concentration C_{L0} shown in Table 3. The trap site concentration increases with loading from initially 1.55×10^{-12} to $1.31 \times 10^{-11} \text{ mol/mm}^3$. This indicates that

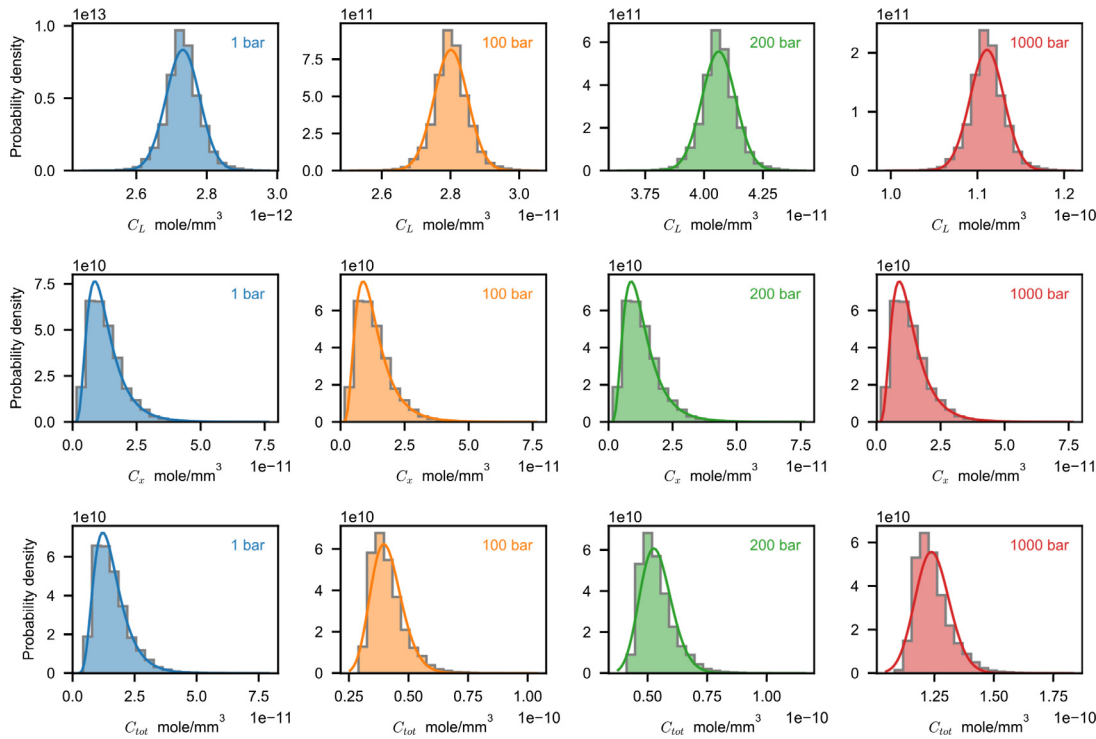


Fig. 5. The probability density distribution of hydrogen in the RVE for different hydrogen pressures. From top to bottom are lattice, trap and total concentrations respectively. The hydrogen pressure increases from left to right.

tensile loading does not affect C_L uptake, rather it only leads to its redistribution. On the contrary, tensile loading significantly affects C_x uptake. Indeed, it was reported that tensile loading has negligible effect on C_L uptake and only affects C_x uptake for iron [57,58]. Following Di Leo and Anand [59], Díaz *et al.* [48] and Martínez-Pañeda *et al.* [60] used constant chemical potential boundary conditions instead of constant concentration. The dependence of hydrogen solubility on hydrostatic stress in their formulation showed an increased C_L . We believe that this will have a minor effect on C_L uptake in our model. Unlike their local evaluation of C_L at a blunting crack tip, we evaluate C_L uptake throughout the whole RVE with heterogeneous stress distribution. Nevertheless, the effect of boundary conditions on C_L uptake within a RVE will be thoroughly investigated in our future studies, especially on hydrogen partitioning.

Another way of modeling the interaction of fracture and hydrogen diffusion is to model a discrete fatigue crack tip. However, the diameter of a fatigue crack tip is the same size or smaller than a single grain in the present simulation. We chose to model an RVE in order to capture a homogenized response of the microstructure and to avoid the possibility that the results depend entirely on the behavior of one or two grains located at the crack tip. It is worth noting that some references that use cracks feature an assumed continuum [59–61] as opposed to a microstructural model.

Applied state of stress and total strain are also important loading parameters. Increasing the far-field strain beyond 3% will increase both concentrations, especially the dislocation-trapped hydrogen. Increasing the stress triaxiality from the plane strain condition presented here to that of a notch or crack tip would increase the hydrostatic tension and therefore increase the C_L . Cracks are also a critical area for hydrogen embrittlement. Strain, stress, and stress state gradient will also dramatically affect the hydrogen distribution, as it will inherently be drawn to areas of high stress triaxiality and plastic strain.

Having described the effect of the charging pressure on C_x and C_L , we now discuss the implications on the total concentration C_{tot} shown in Fig. 6. At 1 bar, the distribution and magnitudes are very similar to the distribution of C_x . This can be confirmed from the last row of Fig. 5. The distribution of C_{tot} has a log-normal distribution with values order of magnitude larger than C_L indicating that at low pressures, the hydrogen distribution is dominated by the trapped hydrogen. With increasing hydrogen pressure, the effect of C_L becomes more tangible. This can be seen from the change in the distribution and magnitudes of C_{tot} in Fig. 6(a) through (d). This can also be seen from Fig. 5 where the shape of the distribution changes from log-normal toward more normal distribution, i.e. more relative contribution of C_L . The spread of the distribution indicates the level of heterogeneity of hydrogen [31]. Increasing hydrogen pressure increases the heterogeneity of hydrogen, and thus, increases the susceptibility to HE.

The micromechanical stress state results in high local concentration of C_L and C_x at triple points and grain boundaries, respectively. Since the initiation of hydrogen cracking is triggered by a hydrogen concentration threshold [62,63], these regions are likely to contribute to fracture given appropriate conditions. Connolly *et al.* [8] discussed that the trapped hydrogen at the grain boundaries due to dislocation pile up can lead to a HEDE mediated HELP damage mechanism. This behaviour will become more prominent with an increasing hydrogen content. This argument can be supported by the experimental observations reporting an increase in the fraction of intergranular fracture with an increase in the hydrogen content [64,65]. Ayas *et al.* [34] analysed the effect of lattice and trapped hydrogen at different trap sites on the failure of AISI 4135 steel. They concluded that intergranular fracture doesn't correlate with grain boundary hydrogen, and its physical basis needs to be elucidated. Our results show that the micromechanical stress state, even in the absence of grain boundary trapping, can result in the accumulation of hydrogen at the grain boundaries. To dis-

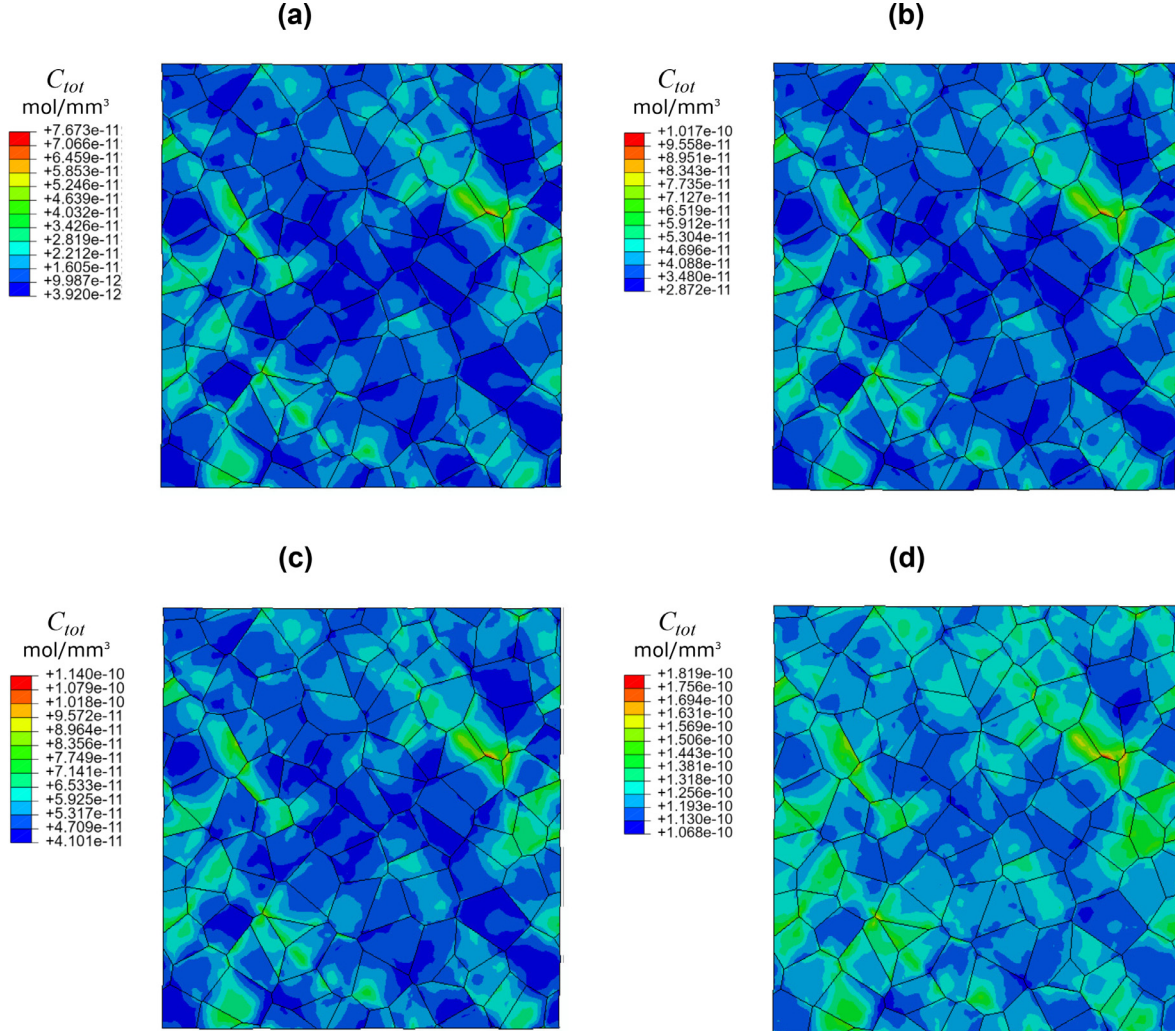


Fig. 6. Total hydrogen distribution ($C_{tot} = C_L + C_x$) after 3×10^{-2} tensile strain loading corresponding to hydrogen pressure of (a) 1 bar, (b) 100 bar, (c) 200 bar and (d) 1000 bar.

cern the effect of different hydrogen populations at grain boundaries, RVE modeling of boundary trapping [66] with appropriate representation of grain boundary character is being considered for future work.

3.2. Effect of yield strength

In this section, we describe the effect of yield strength on the redistribution of hydrogen. Here we used yield strength similar to AISI 4340. The crystal plasticity parameters were calibrated by fitting a stress-strain curve as in [67]. For simplicity, we use the parameters in Table 2 for the mass-transport formulation in section 2.4. We call this hypothetical material high strength steel (HSS). The stress-strain curve from a RVE with these fitted parameters compared to α -iron is shown in Fig. 7.

The redistribution of hydrogen due to the heterogeneous micromechanical stresses in HSS with increasing hydrogen pressure follows a very similar trend as that discussed in section 3.1. In Fig. 8, we only show the hydrogen distribution at 1000 bar of hydrogen pressure for brevity. Fig. 8(a) shows that C_L accumulates in the same regions as those for α -iron in Fig. 4(b). This is to be expected as the only variable we changed in the model was the constitutive behavior, while the microstructure features were kept identical. In fact, this is an advantage of computational models which provide total control over the parameters used in com-

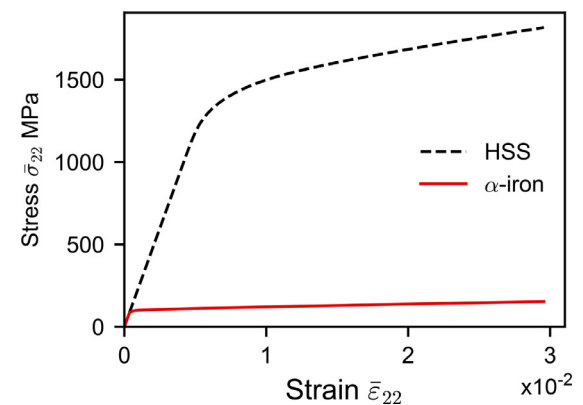


Fig. 7. Stress strain curves using a RVE from calibration of crystal plasticity parameters for HSS and α -iron.

parative studies. The magnitudes of the maximum C_L regions are approximately three times larger than in α -iron, while the minimum regions are three times less. This is due to the higher yield strength of HSS, which develops larger tensile and compressive hydrostatic stresses. C_x shown in Fig. 8(b) also shows similar distribution as in Fig. 4(d), however, the maximum value in HSS is

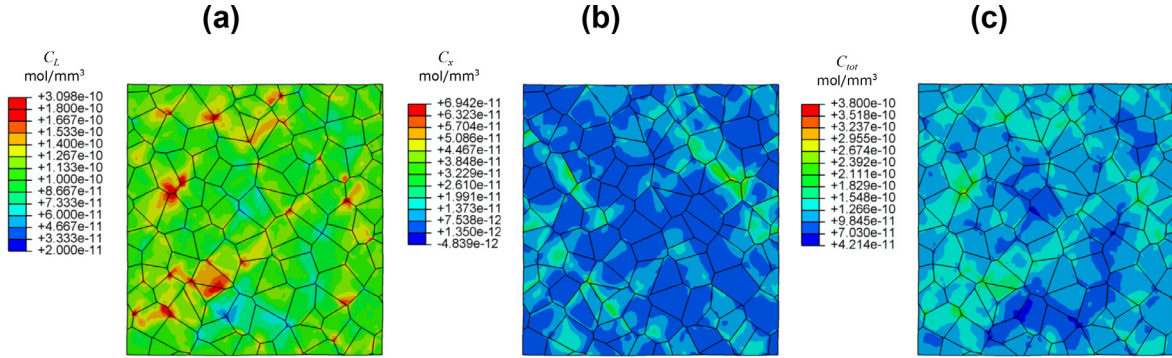


Fig. 8. The distribution of hydrogen in a RVE for HSS at 1000 bar of hydrogen pressure after 3×10^{-2} tensile strain.

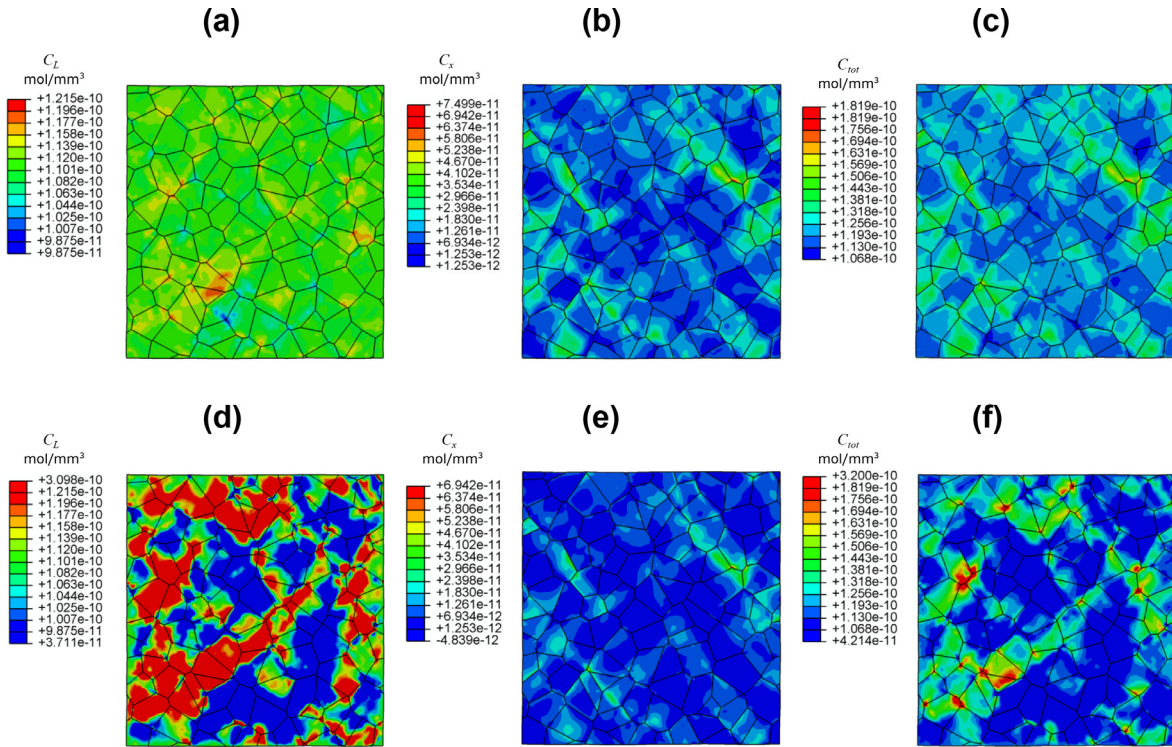


Fig. 9. The distribution of hydrogen for α -iron (a-c) and HSS (d-f) at 1000 bar of hydrogen pressure after 3×10^{-2} tensile strain. The range of the color map is kept constant for a better visualization of the effect of the yield strength.

relatively smaller than that in α -iron. This is due to the relatively smaller values of plastic strains in HSS. Although in both cases the displacement boundary conditions are the same, the plastic strains developing within the individual grains of the RVE are smaller due to the higher yield strength in HSS as shown in Fig. 7.

To put the numbers in perspective, in Fig. 9 we plot the hydrogen distribution for α -iron and HSS with the same limits in the color map. It can be clearly seen that the amount of C_L is much larger for HSS than α -iron. Furthermore, the regions with lower C_L are more depleted for HSS. This larger heterogeneity can be seen from superimposing the fitted distributions as shown in the first row of Fig. 10. HSS has a RSD of 17.3%, i.e. 10 times more than for α -iron. Although we used the same RVE and hydrogen diffusion parameters in both cases, we expected that the lattice hydrogen uptake, i.e. the mean values of C_L , will increase due to increased hydrostatic stresses resulting from increasing the yield strength. Our results show that higher yield strength doesn't lead to increasing the lattice hydrogen uptake, rather, it leads to larger heterogeneity in its distribution. On the other side, trapped

hydrogen in HSS has less heterogeneity and lower mean value of $8.35 \times 10^{-12} \text{ mol/mm}^3$ compared to $1.31 \times 10^{-11} \text{ mol/mm}^3$ α -iron. C_{tot} has lower mean values and larger heterogeneity as can be seen in Fig. 9(f) and the last row in Fig. 10. Therefore higher yield strength surprisingly results in lower hydrogen uptake. However, it effectively increases the hydrogen distribution heterogeneity mainly due to lattice hydrogen. In this case, trapped hydrogen has less relative contribution.

Although the RVE we used represents a single phase microstructure, high strength steels are characterized by having multiple phases like carbides and/or martensite. These hard phases are expected to behave as stress concentration regions that would facilitate damage initiation and propagation due to hydrogen [29]. This was shown both in modeling [68] and experimental [69] studies. Other experimental studies showed a higher hydrogen concentration at martensite and carbide particles [21]. Thus, our approach for using an idealized microstructure can be thought of as a lower-bound with respect to hydrogen content.

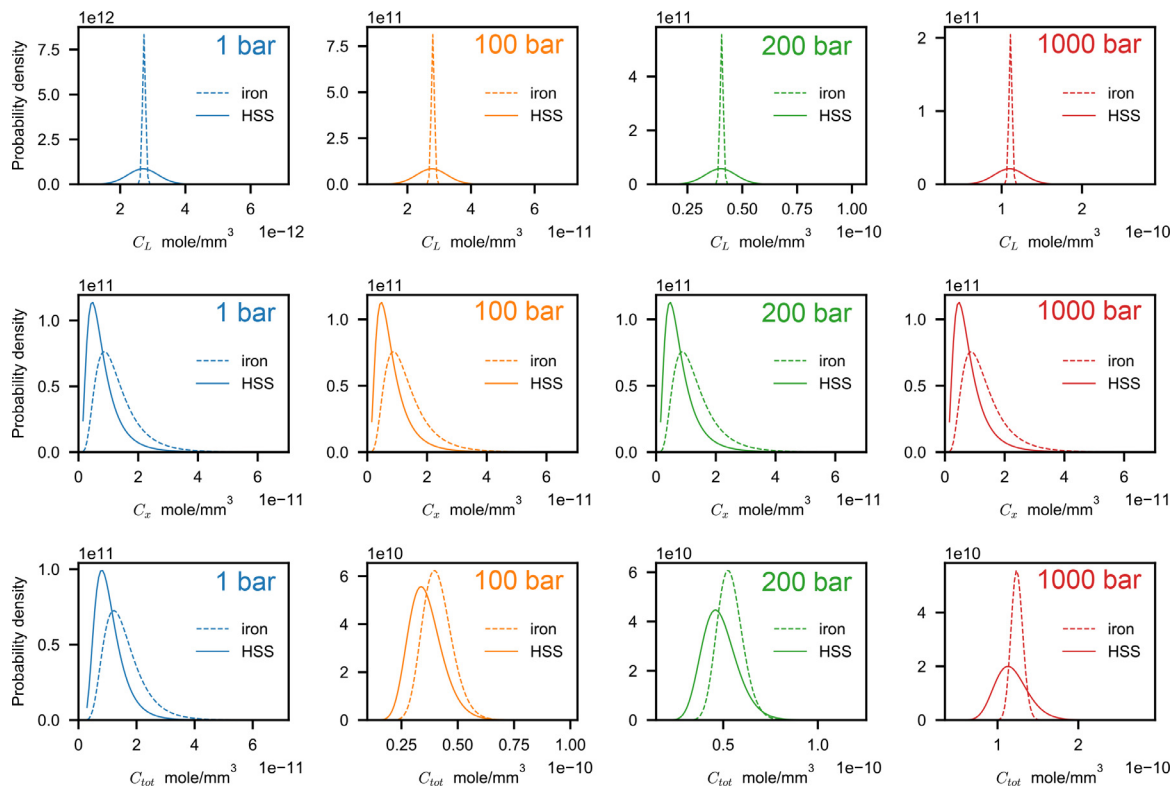


Fig. 10. Comparison between the probability density distribution of hydrogen in α -iron and HSS for different hydrogen pressures.

4. Conclusions

In this work we used a representative volume element (RVE) and a diffusion coupled crystal plasticity model to investigate the effect of micromechanical stresses on the redistribution of lattice (C_L) and dislocation trapped (C_x) hydrogen concentrations in α -iron. The model represented a precharged sample subjected to a constant hydrogen gas pressure. A uniaxial loading was applied to the RVE under plane strain conditions. The redistribution of the hydrogen after loading is due to the micromechanical anisotropy and the random orientations applied to the grains. Furthermore, we studied the effect of increased yield stress in order to represent a scenario for high strength steel. Our main findings are:

- Both C_L and C_x were found to accumulate at the grain boundaries. This suggests that in the absence of grain boundary trapping, the heterogeneity of the micromechanical stress fields leads to the accumulation of hydrogen at the grain boundaries. The competition between grain boundary trapping and heterogeneity of micromechanical stress fields will be the subject of future studies.
- According to Sieverts law, the initial C_L uptake is a function of the hydrogen gas pressure. After applying the load, C_L redistributes according to the hydrostatic stress fields, where it depletes from compressive regions and diffuses toward tensile ones. The hydrostatic stress fields had a negligible effect on the uptake of C_L . On the other side, the hydrogen gas pressure had a negligible effect on the uptake of C_x . Instead, C_x was found to be strongly dependent on the plastic deformation levels. In order to generalize this behaviour, further studies on the effect of the trap binding energy, loading state and strain hardening behaviour are required.

- Our results show that at low hydrogen gas pressure, C_x dominates C_{tot} . The contribution of C_L to C_{tot} increases with increasing the hydrogen gas pressure.

- Higher yield strength had a negligible effect on the uptake of C_L compared to the lower yield strength case. Rather, it led to an increase in the heterogeneity of the redistribution of C_L . Higher yield strength resulted in increasing the localized hydrostatic tensile and compressive stresses. The tensile regions were more enriched in hydrogen, while the compressive zones were more depleted. On the other side, higher yield strength resulted in lower C_x . This is due to the lower plastic deformation levels associated with higher yield strength. Therefore, the increased heterogeneity of the redistribution of C_L can be one of the reasons behind the increased susceptibility to hydrogen embrittlement observed for materials with high yield strength.

Declaration of Competing Interest

The authors declare that they have no known competing financial interests or personal relationships that could have appeared to influence the work reported in this paper.

Acknowledgement

The authors from Delft University of Technology greatly acknowledge the financial support provided within the Cohesion grant by the 3mE faculty of Delft University of Technology.

Appendix A. Details of calculating hydrostatic stress gradient $\nabla\sigma_H$

In this section, we describe the method for calculating the hydrostatic stress gradients $\nabla\sigma_H$ for the coupled temperature-displacement element CPE6MT in ABAQUS. It is based on the pro-

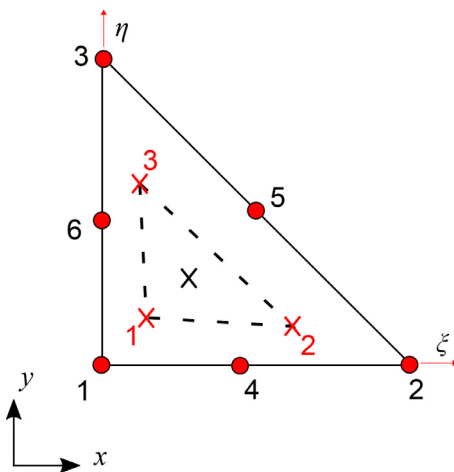


Fig. A.1. The numbering of nodal and integration points for CPE6MT elements in ABAQUS. The dashed triangle represents the pseudo-element with its centroid as integration point.

cedure used to obtain strain gradients for strain gradient plasticity [70–72] and other studies implementing the hydrogen transport model used in this study [6,48,49]. In this procedure, the integration points of a second-order element are assumed to be nodal points of a pseudo-element as shown by the dashed triangle in Fig. A.1. The shape functions of these pseudo-nodes in the natural coordinate system (ξ, η) and their derivatives evaluated at the centroid $(\xi, \eta) = (0, 0)$ are

$$\begin{aligned} N^{(1)} &= 1 - \xi - \eta, & \frac{\partial N^{(1)}}{\partial \xi} &= -1, & \frac{\partial N^{(1)}}{\partial \eta} &= -1 \\ N^{(2)} &= \xi, & \frac{\partial N^{(2)}}{\partial \xi} &= 1, & \frac{\partial N^{(2)}}{\partial \eta} &= 0 \\ N^{(3)} &= \eta, & \frac{\partial N^{(3)}}{\partial \xi} &= 0, & \frac{\partial N^{(3)}}{\partial \eta} &= 1 \end{aligned} \quad (\text{A.1})$$

where the superscript represents the numbering order as shown in Fig. A.1. The values of the hydrostatic stresses σ_H in all these integration points and their coordinates are stored in a Fortran COMMON block declared in the UMAT subroutine. Following the standard FEM procedures, the gradients of these pseudo-nodes are calculated as

$$\left[\begin{array}{c} \frac{\partial \sigma_H}{\partial x} \\ \frac{\partial \sigma_H}{\partial y} \end{array} \right] = \left[\begin{array}{ccc} \frac{\partial N^{(1)}}{\partial x} & \frac{\partial N^{(2)}}{\partial x} & \frac{\partial N^{(3)}}{\partial x} \\ \frac{\partial N^{(1)}}{\partial y} & \frac{\partial N^{(2)}}{\partial y} & \frac{\partial N^{(4)}}{\partial y} \end{array} \right] \left[\begin{array}{c} \sigma_H^{(1)} \\ \sigma_H^{(2)} \\ \sigma_H^{(3)} \end{array} \right] \quad (\text{A.2})$$

where the first term on the right hand side is the gradient matrix. This matrix can be calculated using the inverse of the Jacobian matrix as

$$\left[\begin{array}{c} \frac{\partial N^{(i)}}{\partial x} \\ \frac{\partial N^{(i)}}{\partial y} \end{array} \right] = \left[\begin{array}{cc} \sum_{n=1}^3 \frac{\partial N^{(i)}}{\partial \xi} x_i & \sum_{n=1}^3 \frac{\partial N^{(i)}}{\partial \xi} y_i \\ \sum_{n=1}^3 \frac{\partial N^{(i)}}{\partial \eta} x_i & \sum_{n=1}^3 \frac{\partial N^{(i)}}{\partial \eta} y_i \end{array} \right]^{-1} \left[\begin{array}{c} \frac{\partial N^{(i)}}{\partial \xi} \\ \frac{\partial N^{(i)}}{\partial \eta} \end{array} \right] \quad (\text{A.3})$$

where x_i and y_i are the coordinates of the pseudo-nodes in the global coordinate system. The values of $\nabla \sigma_H$ calculated from Eq. (A.2) are then assigned to the integration points as solution-dependent state variables (SDV) and passed to the UMATHT subroutine.

References

- [1] Government Strategy on Hydrogen Technical Report, Ministry of Economic Affairs and Climate Policy, 2020. URL: <https://www.government.nl/documents/publications/2020/04/06/government-strategy-on-hydrogen>
- [2] M. Steen, Building a hydrogen infrastructure in the EU, in: M. Ball, A. Basile, T.N. Veziroglu (Eds.), Compendium of Hydrogen Energy, Elsevier, 2016, pp. 267–292, doi:[10.1016/B978-1-78242-364-5.00012-9](https://doi.org/10.1016/B978-1-78242-364-5.00012-9).
- [3] M. Nagumo, Fundamentals of Hydrogen Embrittlement, Springer Singapore, Singapore, 2016, doi:[10.1007/978-981-10-0161-1](https://doi.org/10.1007/978-981-10-0161-1).
- [4] O. Barrera, D. Bombac, Y. Chen, T.D. Daff, E. Galindo-Navia, P. Gong, D. Haley, R. Horton, I. Katzarov, J.R. Kermode, C. Liverani, M. Stopher, F. Sweeney, Understanding and mitigating hydrogen embrittlement of steels: a review of experimental, modelling and design progress from atomistic to continuum, Journal of Materials Science 53 (14) (2018) 10593–10594, doi:[10.1007/s10853-018-2291-7](https://doi.org/10.1007/s10853-018-2291-7).
- [5] M.L. Martin, M. Dadfarnia, A. Nagao, S. Wang, P. Sofronis, Enumeration of the hydrogen-enhanced localized plasticity mechanism for hydrogen embrittlement in structural materials, Acta Materialia 165 (2019) 734–750, doi:[10.1016/j.actamat.2018.12.014](https://doi.org/10.1016/j.actamat.2018.12.014). URL: <https://linkinghub.elsevier.com/retrieve/pii/S135964541830956X>
- [6] M.L. Martin, M.J. Connolly, F.W. DelRio, A.J. Slifka, Hydrogen embrittlement in ferritic steels, Applied Physics Reviews 7 (4) (2020), doi:[10.1063/5.0012851](https://doi.org/10.1063/5.0012851).
- [7] M.B. Djukic, G.M. Bakic, V. Sijacki Zeravcic, A. Sedmak, B. Rajacic, The synergistic action and interplay of hydrogen embrittlement mechanisms in steels and iron: Localized plasticity and decohesion, Engineering Fracture Mechanics 216 (2019) 106528, doi:[10.1016/j.engfracmech.2019.106528](https://doi.org/10.1016/j.engfracmech.2019.106528). URL: <https://linkinghub.elsevier.com/retrieve/pii/S0013794418314152>
- [8] M. Connolly, M. Martin, P. Bradley, D. Lauria, A. Slifka, R. Amaro, C. Looney, J.-S. Park, In situ high energy X-ray diffraction measurement of strain and dislocation density ahead of crack tips grown in hydrogen, Acta Materialia 180 (2019) 272–286, doi:[10.1016/j.actamat.2019.09.020](https://doi.org/10.1016/j.actamat.2019.09.020).
- [9] M. Itakura, H. Kaburaki, M. Yamaguchi, T. Okita, The effect of hydrogen atoms on the screw dislocation mobility in bcc iron: A first-principles study, Acta Materialia 61 (18) (2013) 6857–6867, doi:[10.1016/j.actamat.2013.07.064](https://doi.org/10.1016/j.actamat.2013.07.064).
- [10] P. Sofronis, Y. Liang, N. Aravas, Hydrogen induced shear localization of the plastic flow in metals and alloys, European Journal of Mechanics - A/Solids 20 (6) (2001) 857–872, doi:[10.1016/S0997-7538\(01\)01179-2](https://doi.org/10.1016/S0997-7538(01)01179-2).
- [11] P. Novak, R. Yuan, B. Somerd़ay, P. Sofronis, R. Ritchie, A statistical, physical-based, micro-mechanical model of hydrogen-induced intergranular fracture in steel, Journal of the Mechanics and Physics of Solids 58 (2) (2010) 206–226, doi:[10.1016/j.jmps.2009.10.005](https://doi.org/10.1016/j.jmps.2009.10.005). URL: <https://linkinghub.elsevier.com/retrieve/pii/S0022509609001537>
- [12] S. Huang, G. Han, L. Shen, Y. Zhang, Y. Su, L. Qiao, Y. Yan, Influence of hydrogen and annealing process on the microstructural evolution and fracture micromechanisms of medium Mn steel: An in-situ TEM investigation, International Journal of Hydrogen Energy 45 (41) (2020) 22041–22053, doi:[10.1016/j.ijhydene.2020.05.142](https://doi.org/10.1016/j.ijhydene.2020.05.142). URL: <https://linkinghub.elsevier.com/retrieve/pii/S0360319920319443>
- [13] I.M. Robertson, P. Sofronis, A. Nagao, M.L. Martin, S. Wang, D.W. Gross, K.E. Nygren, Hydrogen Embrittlement Understood, Metallurgical and Materials Transactions B 46 (3) (2015) 1085–1103, doi:[10.1007/s11663-015-0325-y](https://doi.org/10.1007/s11663-015-0325-y).
- [14] J. Venezuela, Q. Zhou, Q. Liu, H. Li, M. Zhang, M.S. Dargusch, A. Atrens, The influence of microstructure on the hydrogen embrittlement susceptibility of martensitic advanced high strength steels, Materials Today Communications 17 (2018) 1–14, doi:[10.1016/j.mtcomm.2018.07.011](https://doi.org/10.1016/j.mtcomm.2018.07.011). URL: <https://linkinghub.elsevier.com/retrieve/pii/S235249281830227>
- [15] B. Sun, W. Krieger, M. Rohwerder, D. Ponge, D. Raabe, Dependence of hydrogen embrittlement mechanisms on microstructure-driven hydrogen distribution in medium Mn steels, Acta Materialia 183 (2020) 313–328, doi:[10.1016/j.actamat.2019.11.029](https://doi.org/10.1016/j.actamat.2019.11.029).
- [16] T. Depover, A. Laureys, D.P. Escobar, E. Van den Eeckhout, E. Wallaert, K. Verbecken, Understanding the interaction between a steel microstructure and hydrogen, Materials 11 (5) (2018), doi:[10.3390/ma11050698](https://doi.org/10.3390/ma11050698).
- [17] A.H.M. Krom, A. Bakker, Hydrogen trapping models in steel, Metallurgical and Materials Transactions B 31 (6) (2000) 1475–1482, doi:[10.1007/s11663-000-0032-0](https://doi.org/10.1007/s11663-000-0032-0).
- [18] P. Sofronis, R. McMeeking, Numerical analysis of hydrogen transport near a blunting crack tip, Journal of the Mechanics and Physics of Solids 37 (3) (1989) 317–350, doi:[10.1016/0022-5096\(89\)90002-1](https://doi.org/10.1016/0022-5096(89)90002-1).
- [19] A. Turnbull, Perspectives on hydrogen uptake, diffusion and trapping, International Journal of Hydrogen Energy 40 (47) (2015) 16961–16970, doi:[10.1016/j.ijhydene.2015.06.147](https://doi.org/10.1016/j.ijhydene.2015.06.147).
- [20] R. Oriani, The diffusion and trapping of hydrogen in steel, Acta Metallurgica 18 (1) (1970) 147–157, doi:[10.1016/0001-6160\(70\)90078-7](https://doi.org/10.1016/0001-6160(70)90078-7).
- [21] Y.S. Chen, H. Lu, J. Liang, A. Rosenthal, H. Liu, G. Sneddon, I. McCarroll, Z. Zhao, W. Li, A. Guo, J.M. Cairney, Observation of hydrogen trapping at dislocations, grain boundaries, and precipitates, Science 367 (6474) (2020) 171–175, doi:[10.1126/science.aaz0122](https://doi.org/10.1126/science.aaz0122). URL: <https://science.sciencemag.org/content/367/6474/171>
- [22] M. Koyama, M. Rohwerder, C.C. Tasan, A. Bashir, E. Akiyama, K. Takai, D. Raabe, K. Tsuzaki, Recent progress in microstructural hydrogen mapping in steels: quantification, kinetic analysis, and multi-scale characterisation, Materials Science and Technology (United Kingdom) 33 (13) (2017) 1481–1496, doi:[10.1080/02670836.2017.1299276](https://doi.org/10.1080/02670836.2017.1299276).
- [23] A.J. Breen, L.T. Stephenson, B. Sun, Y. Li, O. Kasian, D. Raabe, M. Herbig, B. Gault, Solute hydrogen and deuterium observed at the near atomic scale in high-strength steel, Acta Materialia 188 (2020) 108–120, doi:[10.1016/j.actamat.2020.02.004](https://doi.org/10.1016/j.actamat.2020.02.004). URL: <https://linkinghub.elsevier.com/retrieve/pii/S1359645420300963>

- [24] A. Krom, R. Koers, A. Bakker, Hydrogen transport near a blunting crack tip, *Journal of the Mechanics and Physics of Solids* 47 (4) (1999) 971–992, doi:10.1016/S0022-5096(98)00064-7.
- [25] R. Fernández-Sousa, C. Betegón, E. Martínez-Pañeda, Analysis of the influence of microstructural traps on hydrogen assisted fatigue, *Acta Materialia* 199 (2020) 253–263, doi:10.1016/j.actamat.2020.08.030. URL: <https://linkinghub.elsevier.com/retrieve/pii/S1359645420306273>
- [26] M. Dadfarnia, M.L. Martin, A. Nagao, P. Sofronis, I.M. Robertson, Modeling hydrogen transport by dislocations, *Journal of the Mechanics and Physics of Solids* 78 (2014) 511–525, doi:10.1016/j.jmps.2015.03.002.
- [27] S. del Busto, C. Betegón, E. Martínez-Pañeda, A cohesive zone framework for environmentally assisted fatigue, *Engineering Fracture Mechanics* 185 (2017) 210–226, doi:10.1016/j.engfracmech.2017.05.021.
- [28] D. Raabe, B. Sun, A. Kwiatkowski Da Silva, B. Gault, H.-W. Yen, K. Sedighiani, P. Thoudenn Sukumar, I.R. Souza Filho, S. Katnagallu, E. Jägle, P. Kürnsteiner, N. Kusumpudi, L. Stephenson, M. Herbig, C.H. Liebscher, H. Springer, S. Zaeferer, V. Shah, S.-L. Wong, C. Baron, M. Diehl, F. Roters, D. Ponge, Current Challenges and Opportunities in Microstructure-Related Properties of Advanced High-Strength Steels, *Metallurgical and Materials Transactions A* 51 (11) (2020) 5517–5586, doi:10.1007/s11661-020-05947-2.
- [29] F. Wei, K. Tsuzaki, Hydrogen trapping phenomena in martensitic steels, in: *Gaseous Hydrogen Embrittlement of Materials in Energy Technologies*, Elsevier, 2012, pp. 493–525, doi:10.1533/9780857093899.3.493. URL: <https://linkinghub.elsevier.com/retrieve/pii/B9781845696771500132>
- [30] S. Bargmann, B. Klusemann, J. Markmann, J.E. Schnabel, K. Schneider, C. Soysal, J. Wilmers, Generation of 3D representative volume elements for heterogeneous materials: A review, *Progress in Materials Science* 96 (2018) 322–384, doi:10.1016/j.jmatsci.2018.02.003.
- [31] D.N. Ilin, N. Saintier, J.M. Olive, R. Abgrall, I. Aubert, Simulation of hydrogen diffusion affected by stress-strain heterogeneity in polycrystalline stainless steel, *International Journal of Hydrogen Energy* 39 (5) (2014) 2418–2422, doi:10.1016/j.ijhydene.2013.11.065.
- [32] H.u. Hassan, K. Govind, A. Hartmaier, Micromechanical modelling of coupled crystal plasticity and hydrogen diffusion, *Philosophical Magazine* 99 (1) (2019) 92–115, doi:10.1080/14786435.2018.1530466.
- [33] Y. Charles, H.T. Nguyen, M. Gaspérini, Comparison of hydrogen transport through pre-deformed synthetic polycrystals and homogeneous samples by finite element analysis, *International Journal of Hydrogen Energy* 42 (31) (2017) 20336–20350, doi:10.1016/j.ijhydene.2017.06.016.
- [34] C. Ayas, V. Deshpande, N. Fleck, A fracture criterion for the notch strength of high strength steels in the presence of hydrogen, *Journal of the Mechanics and Physics of Solids* 63 (1) (2014) 80–93, doi:10.1016/j.jmps.2013.10.002.
- [35] F. Bachmann, R. Hielscher, H. Schaeber, Texture Analysis with MTEX ?? Free and Open Source Software Toolbox, *Solid State Phenomena* 160 (2010) 63–68. 10.4028/www.scientific.net/SSP.160.63
- [36] C. Geuzaine, J.-F. Remacle, Gmsh: A 3-D finite element mesh generator with built-in pre- and post-processing facilities, *International Journal for Numerical Methods in Engineering* 79 (11) (2009) 1309–1331. 10.1002/nme.2579
- [37] R. Quey, P.R. Dawson, F. Barbe, Large-scale 3D random polycrystals for the finite element method: Generation, meshing and remeshing, *Computer Methods in Applied Mechanics and Engineering* 200 (17–20) (2011) 1729–1745, doi:10.1016/j.cma.2011.01.002.
- [38] Y. Hou, S. Cai, T. Sapanathan, A. Dumon, M. Rachik, Micromechanical modeling of the effect of phase distribution topology on the plastic behavior of dual-phase steels, *Computational Materials Science* 158 (November 2018) (2019) 243–254, doi:10.1016/j.commatsci.2018.11.025.
- [39] M. Okereke, S. Keates, *Finite Element Applications*, Springer International Publishing, 2018, doi:10.1007/978-3-319-67125-3.
- [40] W. Tan, F. Naya, L. Yang, T. Chang, B. Falzon, L. Zhan, J. Molina-Aldareguía, C. González, J. Llorca, The role of interfacial properties on the intralaminar and interlaminar damage behaviour of unidirectional composite laminates: Experimental characterization and multiscale modelling, *Composites Part B: Engineering* 138 (2018) 206–221, doi:10.1016/j.compositesb.2017.11.043.
- [41] A. Hussein, B. Kim, Micromechanics based FEM study on the mechanical properties and damage of epoxy reinforced with graphene based nanoplatelets, *Composite Structures* 215 (2019) 266–277, doi:10.1016/j.compstruct.2019.02.059. URL: <https://linkinghub.elsevier.com/retrieve/pii/S0263822318329921>
- [42] Y. Huang, A user-material subroutine incorporating single crystal plasticity in the ABAQUS finite element program, Technical Report, Harvard University, 1991.
- [43] D. Peirce, R. Asaro, A. Needleman, Material rate dependence and localized deformation in crystalline solids, *Acta Metallurgica* 31 (12) (1983) 1951–1976, doi:10.1016/0001-6160(83)90014-7.
- [44] P. Franciosi, L.T. Le, G. Monnet, C. Kahloun, M.H. Chavanne, Investigation of slip system activity in iron at room temperature by SEM and AFM in-situ tensile and compression tests of iron single crystals, *International Journal of Plasticity* 65 (2015) 226–249, doi:10.1016/j.ijplas.2014.09.008.
- [45] J.W. Kysar, Addendum to 'A user-material subroutine incorporating single crystal plasticity in the ABAQUS finite element program, Mech Report 178', Technical Report, Harvard University, 1997.
- [46] A. Kunnick, H. Johnson, Deep trapping states for hydrogen in deformed iron, *Acta Metallurgica* 28 (1) (1980) 33–39, doi:10.1016/0001-6160(80)90038-3.
- [47] C.-S. Oh, Y.-J. Kim, K.-B. Yoon, Coupled Analysis of Hydrogen Transport using ABAQUS, *Journal of Solid Mechanics and Materials Engineering* 4 (7) (2010) 908–917, doi:10.1299/jjmmp.4.908.
- [48] A. Díaz, J. Alegre, I. Cuesta, Coupled hydrogen diffusion simulation using a heat transfer analogy, *International Journal of Mechanical Sciences* 115–116 (2016) 360–369, doi:10.1016/j.ijmecsci.2016.07.020.
- [49] O. Barrera, E. Tarleton, H.W. Tang, A.C. Cocks, Modelling the coupling between hydrogen diffusion and the mechanical behaviour of metals, *Computational Materials Science* 122 (May) (2016) 219–228, doi:10.1016/j.commatsci.2016.05.030.
- [50] Y. Charles, H.T. Nguyen, M. Gaspérini, FE simulation of the influence of plastic strain on hydrogen distribution during an U-bend test, *International Journal of Mechanical Sciences* 120 (December 2016) (2017) 214–224, doi:10.1016/j.ijmecsci.2016.11.017.
- [51] R. Kumar, D.K. Mahajan, Hydrogen distribution in metallic polycrystals with deformation, *Journal of the Mechanics and Physics of Solids* 135 (2020) 103776, doi:10.1016/j.jmps.2019.103776. URL: <https://linkinghub.elsevier.com/retrieve/pii/S0022509619304624>
- [52] A. Sieverts, W. Krumbhaar, Über die Löslichkeit von Gasen in Metallen und Legierungen, *Berichte der deutschen chemischen Gesellschaft* 43 (1) (1910) 893–900, doi:10.1002/cber.191004301152.
- [53] A. Krom, A. Bakker, R. Koers, Modelling hydrogen-induced cracking in steel using a coupled diffusion stress finite element analysis, *International Journal of Pressure Vessels and Piping* 72 (2) (1997) 139–147, doi:10.1016/S0308-0161(97)00019-7.
- [54] J.R. Sims, Standards and codes to control hydrogen-induced cracking in pressure vessels and pipes for hydrogen gas storage and transport, *Gaseous Hydrogen Embrittlement of Materials in Energy Technologies: The Problem, its Characterisation and Effects on Particular Alloy Classes* (2012) 177–192, doi:10.1533/9780857093899.1.177.
- [55] T.C. Cui, P.F. Liu, C.H. Gu, Finite element analysis of hydrogen diffusion/plasticity coupled behaviors of low-alloy ferritic steel at large strain, *International Journal of Hydrogen Energy* 42 (31) (2017) 20324–20335, doi:10.1016/j.ijhydene.2017.06.059. URL: <https://linkinghub.elsevier.com/retrieve/pii/S0360319917323297>
- [56] E. Martínez-Pañeda, S. Del Busto, C.F. Niordson, C. Betegón, Strain gradient plasticity modeling of hydrogen diffusion to the crack tip, *International Journal of Hydrogen Energy* 41 (24) (2016) 10265–10274, doi:10.1016/j.ijhydene.2016.05.014.
- [57] H. Shoda, H. Suzuki, K. Takai, Y. Hagiwara, Hydrogen Desorption Behavior of Pure Iron and Inconel 625 during Elastic and Plastic Deformation, *ISIJ International* 50 (1) (2010) 115–123, doi:10.2355/isijinternational.50.115.
- [58] U. Hadam, T. Zakroczymski, Absorption of hydrogen in tensile strained iron and high-carbon steel studied by electrochemical permeation and desorption techniques, *International Journal of Hydrogen Energy* 34 (5) (2009) 2449–2459, doi:10.1016/j.ijhydene.2008.12.088. URL: <https://linkinghub.elsevier.com/retrieve/pii/S03603199090000135>
- [59] C.V. Di Leo, L. Anand, Hydrogen in metals: A coupled theory for species diffusion and large elastic-plastic deformations, *International Journal of Plasticity* 43 (2013) 42–69, doi:10.1016/j.ijplas.2012.11.005.
- [60] E. Martínez-Pañeda, A. Díaz, L. Wright, A. Turnbull, Generalised boundary conditions for hydrogen transport at crack tips, *Corrosion Science* 173 (2020) 108698, doi:10.1016/j.corsci.2020.108698. URL: <https://linkinghub.elsevier.com/retrieve/pii/S0010938X20305345>
- [61] A. Díaz, I. Cuesta, C. Rodríguez, J. Alegre, Influence of non-homogeneous microstructure on hydrogen diffusion and trapping simulations near a crack tip in a welded joint, *Theoretical and Applied Fracture Mechanics* 112 (2021) 102879, doi:10.1016/j.tafmec.2020.102879. URL: <https://linkinghub.elsevier.com/retrieve/pii/S0167844220304559>
- [62] S. Wang, M.L. Martin, I.M. Robertson, P. Sofronis, Effect of hydrogen environment on the separation of Fe grain boundaries, *Acta Materialia* 107 (2016) 279–288, doi:10.1016/j.actamat.2016.01.067.
- [63] A. Trautmann, G. Mori, M. Oberndorfer, S. Bauer, C. Holzer, C. Dittmann, Hydrogen Uptake and Embrittlement of Carbon Steels in Various Environments, *Materials* 13 (16) (2020) 3604, doi:10.3390/ma13163604.
- [64] M. Wang, E. Akiyama, K. Tsuzaki, Effect of hydrogen on the fracture behavior of high strength steel during slow strain rate test, *Corrosion Science* 49 (11) (2007) 4081–4097, doi:10.1016/j.corsci.2007.03.038. URL: <https://linkinghub.elsevier.com/retrieve/pii/S0010938X07001035>
- [65] T.T. Nguyen, H.M. Heo, J. Park, S.H. Nahm, U.B. Beak, Damage assessment and mechanical performance of Cr-Mo steel used in hydrogen storage vessels, *Engineering Failure Analysis* (2020) 105031, doi:10.1016/j.engfailanal.2020.105031.
- [66] A. Díaz, I.I. Cuesta, E. Martínez-Pañeda, J.M. Alegre, Analysis of hydrogen permeation tests considering two different modelling approaches for grain boundary trapping in iron, *International Journal of Fracture* 223 (1–2) (2019) 17–35, doi:10.1007/s10704-019-00411-8.
- [67] J.J. Rimoli, M. Ortiz, A three-dimensional multiscale model of intergranular hydrogen-assisted cracking, *Philosophical Magazine* 6435 (21) (2010) 2939–2963, doi:10.1080/14786431003752134.
- [68] O. Barrera, E. Tarleton, A. Cocks, A micromechanical image-based model for the featureless zone of Fe??Ni dissimilar weld, *Philosophical Magazine* 94 (12) (2014) 1361–1377, doi:10.1080/14786435.2014.886023.
- [69] M. Koyama, C.C. Tasan, E. Akiyama, K. Tsuzaki, D. Raabe, Hydrogen-assisted decohesion and localized plasticity in dual-phase steel, *Acta Materialia* 70 (2014) 174–187, doi:10.1016/j.actamat.2014.01.048.
- [70] S. Qu, Y. Huang, G. Pharr, K. Hwang, The indentation size effect in the spherical indentation of iridium: A study via the conventional theory of mechanism-based strain gradient plasticity, *International Journal of Plasticity*

- ity 22 (7) (2006) 1265–1286, doi:[10.1016/j.ijplas.2005.07.008](https://doi.org/10.1016/j.ijplas.2005.07.008). URL: <https://linkinghub.elsevier.com/retrieve/pii/S0749641905001440>
- [71] E. Martínez-Pañeda, C. Betegón, Modeling damage and fracture within strain-gradient plasticity, International Journal of Solids and Structures 59 (2015) 208–215, doi:[10.1016/j.ijsolstr.2015.02.010](https://doi.org/10.1016/j.ijsolstr.2015.02.010). URL: <https://linkinghub.elsevier.com/retrieve/pii/S0020768315000505>
- [72] Y.F. Gao, B.C. Larson, J.H. Lee, L. Nicola, J.Z. Tischler, G.M. Pharr, Lattice Rotation Patterns and Strain Gradient Effects in Face-Centered-Cubic Single Crystals Under Spherical Indentation, Journal of Applied Mechanics 82 (6) (2015) 36–38, doi:[10.1115/1.4030403](https://doi.org/10.1115/1.4030403).